

# Room-Temperature Photoluminescence Mediated by Sulfur Vacancies in 2D Molybdenum Disulfide

Yiru Zhu, Juhwan Lim, Zhepeng Zhang, Yan Wang,\* Soumya Sarkar, Hugh Ramsden, Yang Li, Han Yan, Dibya Phuyal, Nicolas Gauriot, Akshay Rao, Robert L. Z. Hoye, Goki Eda, and Manish Chhowalla\*



Cite This: *ACS Nano* 2023, 17, 13545–13553



Read Online

ACCESS |



Metrics & More



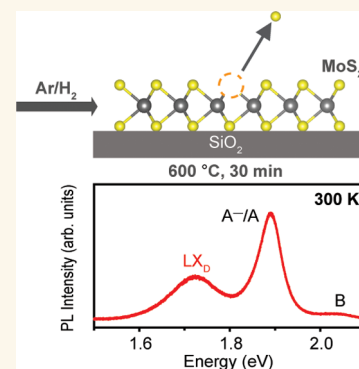
Article Recommendations



Supporting Information

**ABSTRACT:** Atomic defects in monolayer transition metal dichalcogenides (TMDs) such as chalcogen vacancies significantly affect their properties. In this work, we provide a reproducible and facile strategy to rationally induce chalcogen vacancies in monolayer MoS<sub>2</sub> by annealing at 600 °C in an argon/hydrogen (95%/5%) atmosphere. Synchrotron X-ray photoelectron spectroscopy shows that a Mo 3d<sub>5/2</sub> core peak at 230.1 eV emerges in the annealed MoS<sub>2</sub> associated with nonstoichiometric MoS<sub>x</sub> (0 < x < 2), and Raman spectroscopy shows an enhancement of the ~380 cm<sup>-1</sup> peak that is attributed to sulfur vacancies. At sulfur vacancy densities of ~1.8 × 10<sup>14</sup> cm<sup>-2</sup>, we observe a defect peak at ~1.72 eV (referred to as LX<sub>D</sub>) at room temperature in the photoluminescence (PL) spectrum. The LX<sub>D</sub> peak is attributed to excitons trapped at defect-induced in-gap states and is typically observed only at low temperatures (≤77 K). Time-resolved PL measurements reveal that the lifetime of defect-mediated LX<sub>D</sub> emission is longer than that of band edge excitons, both at room and low temperatures (~2.44 ns at 8 K). The LX<sub>D</sub> peak can be suppressed by annealing the defective MoS<sub>2</sub> in sulfur vapor, which indicates that it is possible to passivate the vacancies. Our results provide insights into how excitonic and defect-mediated PL emissions in MoS<sub>2</sub> are influenced by sulfur vacancies at room and low temperatures.

**KEYWORDS:** monolayer molybdenum disulfide, sulfur vacancy generation, room-temperature defect-mediated emission, long-lived localized exciton, sulfur vacancy passivation



Monolayer or two-dimensional transition metal dichalcogenide (2D TMD) semiconductors have strong light–matter interactions.<sup>1,2</sup> This results in high absorption coefficients,<sup>3</sup> photoluminescence (PL) from tightly bound excitons,<sup>4</sup> and valley-selective circular dichroism due to their noncentrosymmetric crystal structure.<sup>5</sup> Further, van der Waals interlayer interactions allow the creation of vertical heterostructures with tunable optoelectronic phenomena.<sup>6</sup> As a result, 2D TMDs are interesting for electronic devices, photovoltaics, and nanophotonics.<sup>7</sup> However, monolayer TMDs prepared by mechanical exfoliation or chemical vapor deposition (CVD) possess a native defect density of ~10<sup>13</sup> cm<sup>-2</sup>.<sup>8,9</sup> These defects are mostly chalcogen vacancies that cause changes in electronic structure by forming in-gap states and carrier doping.<sup>10,11</sup> Monolayer TMDs are surprisingly tolerant of chalcogen vacancy defects. That is, they can host up to 1 × 10<sup>15</sup> cm<sup>-2</sup> chalcogen vacancies without significant distortion to their atomic structure.<sup>12</sup> Above this concentration, however, significant damage to the structure occurs, and disordered regions start to appear. Various approaches to generate defects, such as *in vacuo* annealing,<sup>13</sup>

electron beam irradiation,<sup>14</sup> focused X-ray beam irradiation,<sup>15,16</sup> and focused ion beam exposure,<sup>17,18</sup> have been reported. Controlled defect creation in 2D TMDs can induce single photon emission,<sup>19,20</sup> enhance electro-/photocatalysis,<sup>21,22</sup> and enable sensing.<sup>23</sup> However, defects reduce the performance of electronic devices<sup>24</sup> and therefore require minimization or effective passivation.<sup>25,26</sup>

One way to investigate changes in the electronic structure of 2D TMD semiconductors due to vacancy defects is to characterize the absorption and PL from defect-induced in-gap states. Absorption from such defect states has been observed at room temperature (RT ~300 K),<sup>27</sup> whereas light emission is typically observed at low temperatures at which

**Received:** March 6, 2023

**Accepted:** July 3, 2023

**Published:** July 7, 2023



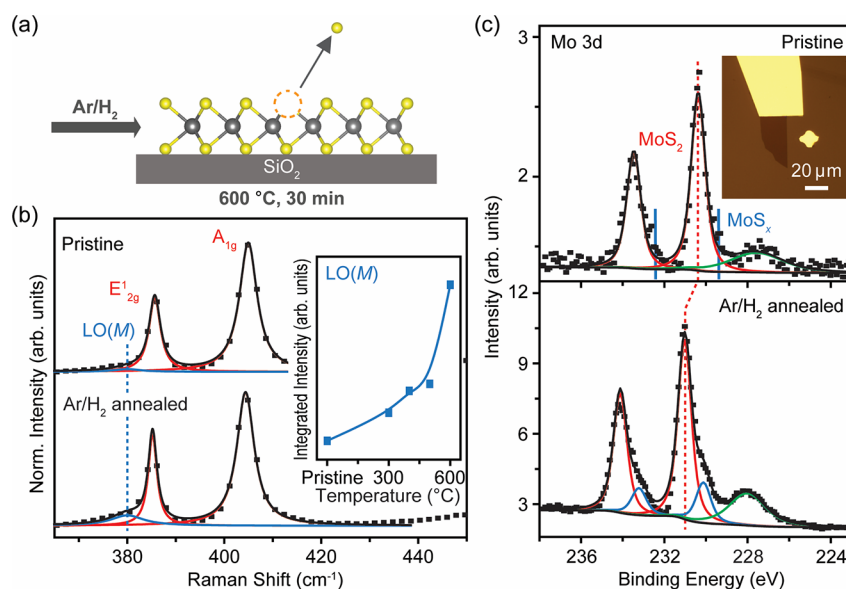


**Figure 1.** Defect generation in monolayer MoS<sub>2</sub> by annealing in an Ar/H<sub>2</sub> (95%/5%) atmosphere. (a) Schematic of sulfur vacancy generation through Ar/H<sub>2</sub> annealing. (b) Raman spectra of pristine and 600 °C Ar/H<sub>2</sub> annealed MoS<sub>2</sub>, normalized to the intensity of the Si reference peak. Pristine MoS<sub>2</sub> shows an E<sub>2g</sub><sup>1</sup> in-plane mode and an A<sub>1g</sub> out-of-plane mode. The low-frequency shoulder on the left of the E<sub>2g</sub><sup>1</sup> mode indicates the LO(M) defect mode, denoted in blue. The increased intensity of the defect mode in the annealed MoS<sub>2</sub> indicates defect generation. Inset: Integrated intensity plot of the LO(M) mode as a function of annealing temperature, ranging from 300 to 600 °C. The intensity increase of the defect mode with annealing temperature indicates an increase in the sulfur vacancy density. (c) XPS spectra of the Mo 3d core level in pristine and 600 °C Ar/H<sub>2</sub> annealed MoS<sub>2</sub>. This measurement was performed by using synchrotron 1 keV soft X-rays. Pristine MoS<sub>2</sub> shows the characteristic doublet from stoichiometric MoS<sub>2</sub> (denoted in red) and S 2s peak (denoted in green). The annealed MoS<sub>2</sub> shows a second Mo 3d doublet from nonstoichiometric MoS<sub>x</sub> (0 < x < 2, denoted in blue), indicating defect generation. Inset: Optical microscopy image of monolayer MoS<sub>2</sub> that is grounded with an In/Au electrode during XPS measurements. Scale bar = 20 μm.

excitons are bound to defect states to facilitate radiative recombination.<sup>28,29</sup> As a result of this strong localization, the defect-mediated emission generally exhibits long lifetimes.<sup>30</sup> In this work, we find that it is possible to observe emission from trapped excitons at RT when defect density ( $n_d$ ) is in the range of  $10^{13} \text{ cm}^{-2} < n_d < 10^{15} \text{ cm}^{-2}$ . We explored the influence of temperature and excitation power on localized emission. Time-resolved PL measurements were also been conducted. Further, we show that sulfur vacancies can be passivated with exposure to sulfur vapor and compare optical properties of defective and passivated samples to gain insight into how concentration of defects influences the optoelectronic properties of monolayer MoS<sub>2</sub>.

## RESULTS AND DISCUSSION

We prepared monolayer MoS<sub>2</sub> samples on SiO<sub>2</sub> substrates by mechanical exfoliation and CVD growth (see the “Experimental Methods” section for details). To generate sulfur vacancies, the samples were annealed in an Ar/H<sub>2</sub> (95%/5%) atmosphere for 30 min (Figure 1a) at temperatures ranging from 300 to 600 °C. We observed a clear change in optical contrast due to material degradation above 600 °C (Supporting Information (SI), Figure S1c). The Raman spectrum of pristine monolayer MoS<sub>2</sub> in Figure 1b shows that it consists of a characteristic E<sub>2g</sub><sup>1</sup> in-plane mode peak at  $\sim 385 \text{ cm}^{-1}$  and A<sub>1g</sub> out-of-plane mode peak at  $\sim 405 \text{ cm}^{-1}$ .<sup>31</sup> The weak satellite peak at  $\sim 380 \text{ cm}^{-1}$  is generally assigned to a longitudinal optical branch (LO(M)) due to sulfur vacancies.<sup>32,33</sup> The intensity of the defect mode was found to increase with annealing from 300–600 °C, indicating that sulfur vacancy density gradually increased with temperature (Figure 1b, inset; see details in SI, Figure S1a). The most

intense LO(M) defect mode was found in 600 °C annealed MoS<sub>2</sub>, indicating that under this condition, the sample contains the highest defect density.

Defect generation in the 600 °C annealed sample was corroborated by chemical analysis using synchrotron X-ray photoelectron spectroscopy (XPS) also termed photoemission spectroscopy (PES) (Figure 1c). The exfoliated monolayer flakes (lateral size of  $\sim 20 \text{ μm}$ , similar to the beam spot size) were grounded using lithographically patterned In/Au electrodes<sup>34</sup> to avoid charging during XPS. To exclude the influence of potential defect generation by synchrotron X-ray radiation, we performed radiation damage tests using synchrotron 3 keV hard X-rays. No obvious changes in the XPS spectra were observed over several measurements at a fixed sample position (SI, Figure S2), indicating that beam-induced defects during measurements can be neglected.

XPS spectra of the Mo 3d doublet were measured using 1 keV soft X-rays as a surface-sensitive probe. Pristine MoS<sub>2</sub> shows the characteristic doublet corresponding to binding energy of stoichiometric MoS<sub>2</sub> at 230.4 eV (Mo 3d<sub>5/2</sub>)<sup>35</sup> (see the Supporting Information for details of XPS fitting procedure). The annealed MoS<sub>2</sub> shows the doublet of stoichiometric MoS<sub>2</sub> at 231.0 eV (Mo 3d<sub>5/2</sub>), as well as peaks from nonstoichiometric MoS<sub>x</sub> (0 < x < 2) at 230.1 eV (Mo 3d<sub>5/2</sub>), respectively. The defect concentration for both pristine and annealed MoS<sub>2</sub> is extracted from stoichiometry calculation, using the core level spectra of Mo 3d and S 2s. The actual stoichiometry is given by

$$\frac{S \text{ (at. \%)}}{Mo \text{ (at. \%)}} = \frac{\left( \frac{I_{S_{2s}}}{\sigma_{S_{2s}}} \right)}{\left( \frac{I_{Mo_{3d_{5/2}}}}{\sigma_{Mo_{3d_{5/2}}}} \right)}$$

Here,  $S \text{ (at. \%)}$  and  $Mo \text{ (at. \%)}$  are the atomic percent (at. %) of S and Mo,  $I_{S_{2s}}$  and  $I_{Mo_{3d_{5/2}}}$  are the integrated intensity of S 2s peak and Mo 3d<sub>5/2</sub> peak.  $\sigma_{S_{2s}}$  and  $\sigma_{Mo_{3d_{5/2}}}$  are the photoionization cross-section at photon energy of 1 keV modeled by Scofield, where  $\sigma_{S_{2s}} = 0.44168$ , and  $\sigma_{Mo_{3d_{5/2}}} = 2.4679$ .<sup>36</sup> For pristine MoS<sub>2</sub>, the actual stoichiometry is calculated to be MoS<sub>1.99</sub>, which leads to a defect concentration of 0.5%. In a perfect superstructure of 1H MoS<sub>2</sub>, the sulfur–sulfur distance is 3.162 Å,<sup>37</sup> thus the density of S atoms in monolayer MoS<sub>2</sub> can be calculated to be  $\sim 2.3 \times 10^{15} \text{ cm}^{-2}$ . For a defect concentration of 0.5%, the defect density is approximated to be  $\sim 1.15 \times 10^{13} \text{ cm}^{-2}$ , similar to reported values on pristine samples.<sup>8</sup> For the annealed MoS<sub>2</sub>, the calculated stoichiometry is MoS<sub>1.84</sub> with a defect concentration of  $\sim 7.7\%$ , equivalent to a sulfur vacancy density of  $\sim 1.8 \times 10^{14} \text{ cm}^{-2}$ . It is worth noting that for the defective sample, the Mo 3d doublet is shifted to higher binding energies by 0.6 eV (as indicated by the dashed vertical red line in Figure 1c), indicating electron doping mediated by sulfur vacancies—consistent with donor states detected by scanning tunneling microscopy/spectroscopy<sup>38</sup> and deep level transient spectroscopy (DLTS).<sup>39</sup>

The defects generated through annealing lead to the formation of electronic in-gap states in monolayer MoS<sub>2</sub>, as shown in the schematic energy band diagram in Figure 2a—consistent with the band structure of sulfur-deficient monolayer MoS<sub>2</sub> by density functional theory (DFT) calculations.<sup>40</sup> We have used PL spectroscopy (Figure 2b; see details in SI, Figure S1b) and reflectance measurements (Figure 2c) to characterize the RT optical properties of monolayer MoS<sub>2</sub>. In pristine MoS<sub>2</sub>, the RT PL spectrum shows the characteristic A<sup>−</sup> trion/A exciton (A<sup>−</sup>/A) peak at 1.90 eV and B exciton peak at 2.05 eV. The reflectance spectrum shows corresponding A (1.91 eV) and B (2.06 eV) excitonic transitions.<sup>41</sup> For the annealed sample, the RT PL spectrum shows a low-energy localized emission peak, LX<sub>D</sub>, that originates from defect-induced in-gap states with a large binding energy of 185 meV. The LX<sub>D</sub> emission results from excitonic transitions between one unoccupied, in-gap defect state lying  $\sim 0.6$  eV below the conduction band minimum (CBM) and the other energy state at the valence band maximum (VBM).<sup>40</sup> For monolayer MoS<sub>2</sub>, the binding energy of A exciton is  $\sim 0.41$  eV. Therefore, the binding energy of defect-mediated emission can be approximated to be  $\sim 190$  meV, which matches the binding energy of 185 meV of LX<sub>D</sub> peak in our PL results. The reflectance spectrum is also broadened in the defective sample. The RT PL spectra were deconvoluted to extract the ratio of integrated intensity of A<sup>−</sup> trion to A exciton,  $I(A^{\cdot-})/I(A)$  (SI, Figure S3a,b).<sup>42</sup> The ratio was found to increase from 0.44 in pristine MoS<sub>2</sub> to 1.06 in annealed MoS<sub>2</sub>, indicating increased electron doping from creation of defects, consistent with the XPS peak shift shown in Figure 1c.

The RT LX<sub>D</sub> emission peak emerges weakly at 500 °C and becomes intense in 600 °C annealed samples (SI, Figure S1b). To understand the role of H<sub>2</sub> in defect generation, we annealed monolayer MoS<sub>2</sub> in an inert Ar-only atmosphere. The Ar-annealed samples did not show LX<sub>D</sub> peaks at RT (see SI,

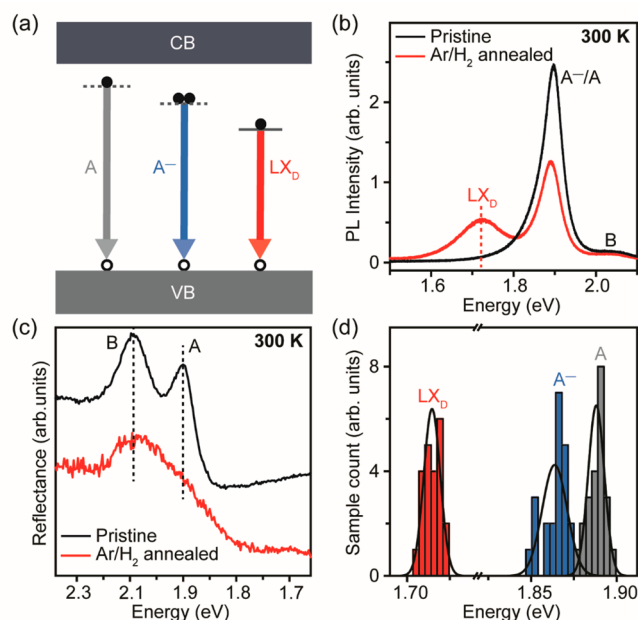


**Figure 2.** RT optical properties induced by sulfur vacancies in monolayer MoS<sub>2</sub>. (a) Proposed schematic energy band diagram of the sulfur-deficient monolayer MoS<sub>2</sub>. The gray arrow (neutral exciton A) represents an electron in the conduction band (CB) recombining with a hole in the valence band (VB). The blue arrow (negative trion A<sup>−</sup>) represents the recombination of two electrons and a hole. The red arrow (LX<sub>D</sub>) represents a localized electron recombining with a hole. The horizontal dashed lines represent virtual energy states, while the solid horizontal line represents real energy states due to defects. (b) RT PL spectra of pristine and 600 °C Ar/H<sub>2</sub> annealed monolayer MoS<sub>2</sub>. Besides the A<sup>−</sup> trion/A exciton (A<sup>−</sup>/A) and B exciton emission shown in the pristine MoS<sub>2</sub> spectrum, the annealed MoS<sub>2</sub> spectrum shows a low-energy localized emission LX<sub>D</sub> mediated by defects, as indicated by the dashed vertical red line. (c) Reflectance spectra of pristine and 600 °C Ar/H<sub>2</sub> annealed monolayer MoS<sub>2</sub>. Pristine MoS<sub>2</sub> spectrum indicates the reflectance signals of the A exciton and B exciton. The broadening reflectance spectrum of the annealed MoS<sub>2</sub> indicates the generation of in-gap defect states. (d) Statistical histogram of emission energy of A, A<sup>−</sup>, and LX<sub>D</sub> emission for 22 individual 600 °C Ar/H<sub>2</sub> annealed samples showing the high consistency and reproducibility of the LX<sub>D</sub> emission.

Figure S4). We also confirm that the RT LX<sub>D</sub> peak is not from the Ar/H<sub>2</sub> annealed SiO<sub>2</sub> substrate (see SI, Figure S5). Our results are reproducible and consistent across 22 samples measured in this study, as shown in the statistical histogram in Figure 2d (see the Supporting Information for details of the steady-state PL fitting procedure).

To understand how the localization of excitons at defect states is related to the evolution of the LX<sub>D</sub> peak, we performed temperature-dependent PL (Figure 3a). For pristine MoS<sub>2</sub> at 10 K, the most intense peak is the LX<sub>N</sub> peak, which is generally attributed to native absorbates<sup>13</sup> accompanied by a weakened A<sup>−</sup>/A peak. In contrast, for the annealed MoS<sub>2</sub>, the most intense emission peak is the LX<sub>D</sub> peak, with the LX<sub>N</sub> and A<sup>−</sup>/A peaks significantly suppressed. The emission energy of LX<sub>D</sub> is consistent with that of sulfur-vacancy-induced emission generated by *in vacuo* annealing,<sup>13</sup> focused He<sup>+</sup> irradiation,<sup>13</sup> and proton irradiation.<sup>30</sup> As the samples were cooled from 300 to 10 K, the dominant recombination pathway shows a transition from A<sup>−</sup>/A to LX<sub>N</sub> emission in the case of pristine MoS<sub>2</sub>. For the annealed sample, the transition from A<sup>−</sup>/A to



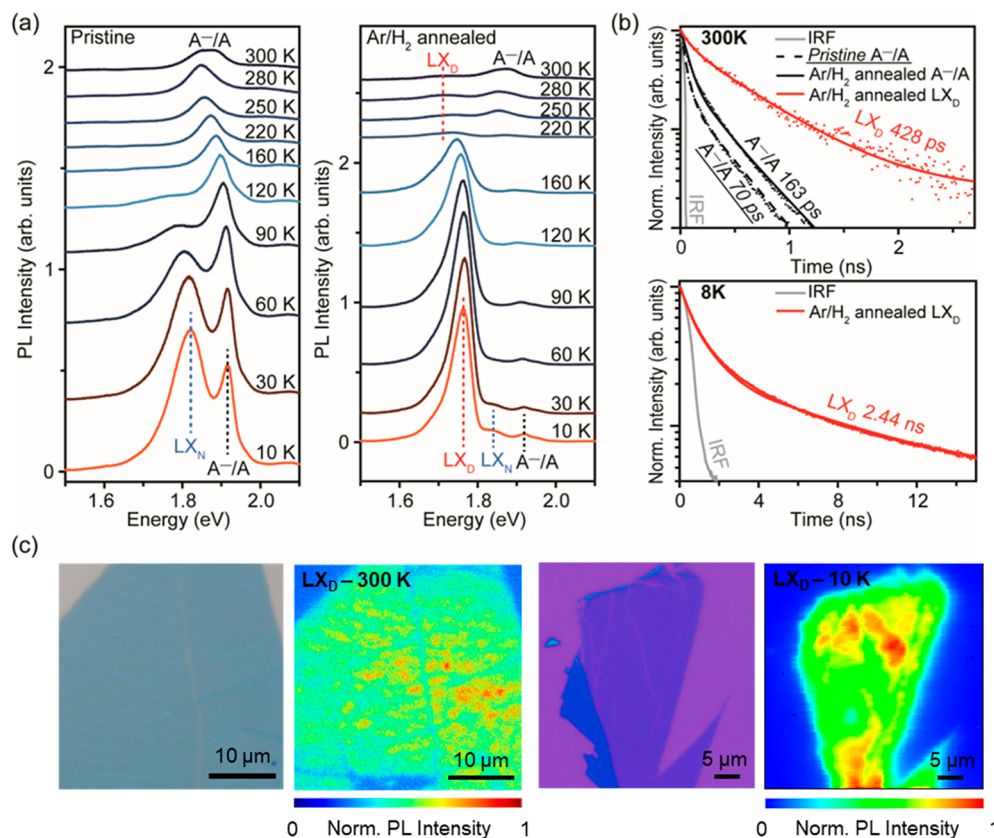


**Figure 3.** In-gap states induced by sulfur vacancies. (a) Temperature-dependent PL spectra of pristine and 600 °C Ar/H<sub>2</sub> annealed monolayer MoS<sub>2</sub>. At 10 K, the LX<sub>N</sub> peak is attributed to native absorbates, while the LX<sub>D</sub> peak is attributed to sulfur vacancies. The continuous increase of LX<sub>N</sub> and LX<sub>D</sub> over the A<sup>-</sup>/A exciton emission with decreasing measurement temperature indicates the temperature-dependent localization of in-gap states. (b) PL decays of pristine and 600 °C Ar/H<sub>2</sub> annealed monolayer MoS<sub>2</sub> measured at 300 and 8 K show longer lifetimes of localized excitons at in-gap states. (c) Intensity maps of LX<sub>D</sub> emission measured at 300 and 10 K, with corresponding optical microscopy images of target flake, showing the distribution of LX<sub>D</sub> emission over the monolayer.

LX<sub>D</sub> emission indicates a strong localization of excitons at lower-lying in-gap states. The absorbates-related emission can be suppressed by full encapsulation in hexagonal boron nitride, as shown in SI, Figure S6.<sup>43–45</sup>

In-gap states trap excitons and subsequently increase their PL decay lifetime.<sup>29,30</sup> We measured the PL decay of the LX<sub>D</sub> emission at 300 and 8 K by time-resolved PL spectroscopy (Figure 3b). At 300 K (Figure 3b, top), pristine MoS<sub>2</sub> shows an A<sup>-</sup>/A exciton lifetime of 70 ps, and the annealed MoS<sub>2</sub> shows a slightly longer A<sup>-</sup>/A exciton lifetime of 163 ps due to the increased electron doping, which results in a larger proportion of trions<sup>46</sup> (see the Supporting Information for details of the time-resolved PL decay fitting procedure). The LX<sub>D</sub> exciton lifetime was measured to be longer, 428 ps. When the sample was cooled to 8 K, the A<sup>-</sup>/A exciton lifetime was below the detection limit of our instrument. In contrast, the LX<sub>D</sub> exciton in annealed MoS<sub>2</sub> was significantly long-lived, with a lifetime of 2.44 ns (Figure 3b, bottom). The long lifetimes of LX<sub>D</sub> excitons support the idea that they are localized at defect sites. To probe the distribution of defects in the annealed MoS<sub>2</sub>, we obtained intensity maps of LX<sub>D</sub> peak at 300 and 10 K (Figure 3c). The LX<sub>D</sub> emission clearly shows consistent spectral characteristics with some variations in the intensity (SI, Figure S7).

To investigate the evolution of LX<sub>D</sub> emission with defect density, we characterized the RT LX<sub>D</sub> emission as a function of the annealing time at 600 °C (Figure 4a,b). In pristine MoS<sub>2</sub>,

in which the density of sulfur vacancies was  $\sim 1.15 \times 10^{13} \text{ cm}^{-2}$ , the LX<sub>D</sub> defect peak was absent. As the annealing time was increased, the LX<sub>D</sub> emission rose in intensity, reaching the maximum at 30 min, where the density of defects was  $\sim 1.8 \times 10^{14} \text{ cm}^{-2}$ , supported through XPS measurements. Increasing the annealing time beyond 30 min results in a decrease in intensity of all spectral features (A<sup>-</sup>/A and LX<sub>D</sub> emission), which could be due to gradual material degradation at higher defect densities. Our previous work on sulfur vacancy generation using focused He<sup>+</sup> irradiation ( $0.24 \text{ kJ/cm}^2$ ) showed that at defect densities  $> 1.5 \times 10^{15} \text{ cm}^{-2}$ , the MoS<sub>2</sub> lattice structure is damaged and the PL is quenched,<sup>12</sup> similar to the sample annealed in Ar/H<sub>2</sub> for 3 h (see Figure 4c). The dependence of the LX<sub>D</sub> emission on defect concentration can be well correlated with the LO(M) defect mode in Raman spectra, and both reach their maximum intensity at an annealing time of 30 min (Figure 4b; see details in SI, Figure S8). Our results suggest that the strongest RT LX<sub>D</sub> emission in 2D MoS<sub>2</sub> occurs at a sulfur vacancy concentration of  $\sim 1.8 \times 10^{14} \text{ cm}^{-2}$ .

We performed power-dependent measurements at 10 K to study how the filling of defect states influences PL properties (Figure 4d). The PL intensity ( $I_{\text{PL}}$ ) follows a power-law dependence with excitation laser power ( $I_{\text{E}}$ ) so that  $I_{\text{PL}} \propto I_{\text{E}}^k$ , where  $k$  is power exponent.<sup>47</sup> Excitonic transitions typically exhibit linear excitation power dependence ( $k = \sim 1$ ), while transitions from localized excitons at lattice defects saturate at

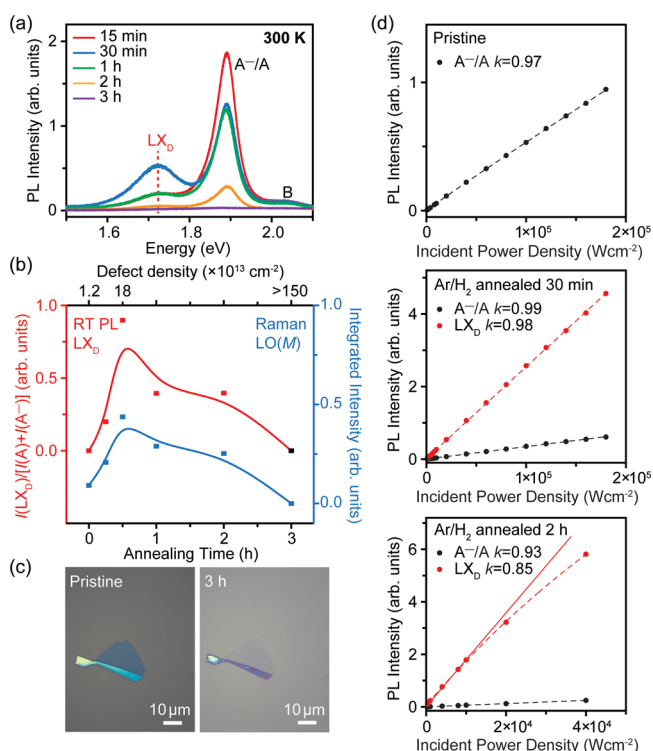


**Figure 4.** Evolution of monolayer MoS<sub>2</sub> with increasing annealing time at 600 °C. (a) RT PL spectra of monolayer MoS<sub>2</sub> with different annealing times. (b) (left) Evolution of integrated RT PL intensity ratio of LX<sub>D</sub> emission to the sum of A exciton and A<sup>-</sup> trion emission, referred to as  $I(\text{LX}_D)/[I(\text{A}) + I(\text{A}^-)]$ . (right) Evolution of the integrated Raman intensity of the LO(M) defect mode. The most intense RT LX<sub>D</sub> emission and LO(M) mode are both observed in 30 min annealed MoS<sub>2</sub>. (c) Optical microscopy images of pristine and 3 h Ar/H<sub>2</sub> annealed monolayer MoS<sub>2</sub> show clear degradation of monolayer MoS<sub>2</sub> through annealing. (d) Power-dependent PL spectra of pristine, 30 min, and 2 h Ar/H<sub>2</sub> annealed monolayer MoS<sub>2</sub> measured at 10 K. A<sup>-</sup>/A shows linear dependence, while LX<sub>D</sub> shows linear dependence in 30 min annealed MoS<sub>2</sub>, whereas saturation dependence in 2 h annealed MoS<sub>2</sub>. The power exponent  $k$  is obtained from fitting of logarithmic plots, where  $k \sim 1$  implies excitonic transition and  $k < 1$  suggests defect-mediated recombination.

higher power values ( $k < 1$ ) due to the finite availability of trap states.<sup>48,49</sup> As shown in Figure 4d, pristine MoS<sub>2</sub> shows a linear dependence of the A<sup>-</sup>/A peak ( $k = 0.97$ , see the logarithmic plot in SI, Figure S9). Similar linear dependence is observed in the A<sup>-</sup>/A peak for the 30 min annealed MoS<sub>2</sub> ( $k = 0.99$ ) and 2 h annealed MoS<sub>2</sub> ( $k = 0.93$ ). While LX<sub>D</sub> shows a linear dependence in the 30 min annealed MoS<sub>2</sub> ( $k = 0.98$ ), the peak shows a clear sublinear behavior in the 2 h annealed MoS<sub>2</sub> ( $k = 0.85$ ), consistent with previous reports.<sup>47,48</sup> The absence of saturation in the power dependence of LX<sub>D</sub> for the 30 min annealed MoS<sub>2</sub> suggests that this material may host more optically active defect sites for radiative recombination, which possibly requires higher excitation fluence to observe saturation. This in fact allows us to observe a clear PL emission from the defect states at RT, in contrast to previous observations of defect-related emission that have mostly been limited to low temperatures (SI, Table S1).

The sulfur vacancies generated by annealing at 600 °C for 30 min in Ar/H<sub>2</sub> give interesting PL properties but are typically detrimental to electronic transport. Thus, there is interest in

passivating them to reduce carrier doping and scattering. We therefore investigated the filling of sulfur vacancies by exposing the defective sample to sulfur vapor at 500 °C (see schematic in Figure 5a). In the XPS spectra of the Mo 3d doublet (Figure 5b), we observe the absence of the nonstoichiometric MoS<sub>x</sub> signal in the MoS<sub>2</sub> samples annealed at 600 °C in Ar/H<sub>2</sub> after annealing in sulfur vapor. The actual stoichiometry after sulfur vapor treatment was found to be MoS<sub>2.05</sub>, comparable to that of the pristine MoS<sub>2</sub> samples. The reflectance spectrum of the passivated sample shown in Figure 5c is similar to that of pristine MoS<sub>2</sub>, with the A and B excitonic edges recovered. In PL spectra at 300 and 10 K, the LX<sub>D</sub> peak is absent for the sulfur passivated sample (Figure 5e). However, XPS results reveal an unusual shift of the Mo 3d doublet in sulfur passivated MoS<sub>2</sub> to higher binding energies of 231.2 eV (Mo 3d<sub>5/2</sub>), which indicates significant electron doping. This can be correlated with the RT PL spectrum, which shows a higher  $I(\text{A}^-)/I(\text{A})$  peak ratio of 2.05 (SI, Figure S3c). The electron doping is likely due to excessive physisorbed sulfur on the surface of MoS<sub>2</sub> during passivation. To confirm this, we measured synchrotron XPS S 1s spectra (Figure 5d), which reveal that Ar/H<sub>2</sub> annealed MoS<sub>2</sub> only shows a pristine S 1s peak at 2475.0 eV, whereas passivated MoS<sub>2</sub> shows two peaks (see the Supporting Information for details of the XPS fitting procedure). The second peak with a lower binding energy of 2473.2 eV can be attributed to physisorbed sulfur on the MoS<sub>2</sub> surface.<sup>50</sup>

We sought to remove the weakly physisorbed sulfur on MoS<sub>2</sub> by annealing the passivated sample at 100 °C under a high vacuum. We chose 100 °C because it is sufficient for subliming unbonded sulfur, but not high enough to create new vacancies.<sup>13</sup> The PL spectra in Figure 5e show that the A<sup>-</sup>/A emission peak is blue-shifted close to the value measured for pristine MoS<sub>2</sub>. Furthermore, the  $I(\text{A}^-)/I(\text{A})$  ratio was decreased to 0.19, indicating that electron doping is largely reduced (SI, Figure S3d). At 10 K, the defect-mediated LX<sub>D</sub> emission reappears, albeit with lower intensity than absorbance-related LX<sub>N</sub> emission, showing that the passivation of in-gap states by annealing in sulfur vapor is a combination of chemical bonding and electron doping. These results show that it is possible to controllably engineer defects and passivate them in both exfoliated and CVD-grown MoS<sub>2</sub> (SI, Figure S10). Having optimized these protocols for MoS<sub>2</sub>, we extended them to other TMDs such as WS<sub>2</sub>, MoSe<sub>2</sub>, and WSe<sub>2</sub>, as shown in SI, Figure S11. Similar RT defect peaks were observed in monolayer WS<sub>2</sub>, while no RT defect peak was observed in selenide monolayer TMDs, including MoSe<sub>2</sub> and WSe<sub>2</sub>.

## CONCLUSION

We have demonstrated that by controlling the temperature, duration, and environment of thermal annealing, we can reproducibly generate sulfur vacancies in 2D MoS<sub>2</sub>. The sulfur vacancies induce in-gap electronic states and lead to RT localized exciton emission that can be tuned by the annealing conditions. We also show that sulfur vacancies can be passivated by annealing in sulfur vapor. Our results provide a simple technique to reproducibly create chalcogen vacancies in wafer-scale TMD films, which may enable functional devices.

## EXPERIMENTAL METHODS

**Sample Preparation. Mechanical Exfoliation.** Monolayer TMDs, including MoS<sub>2</sub>, WS<sub>2</sub>, MoSe<sub>2</sub>, and WSe<sub>2</sub>, were prepared by mechanical exfoliation from commercial bulk crystal purchased from

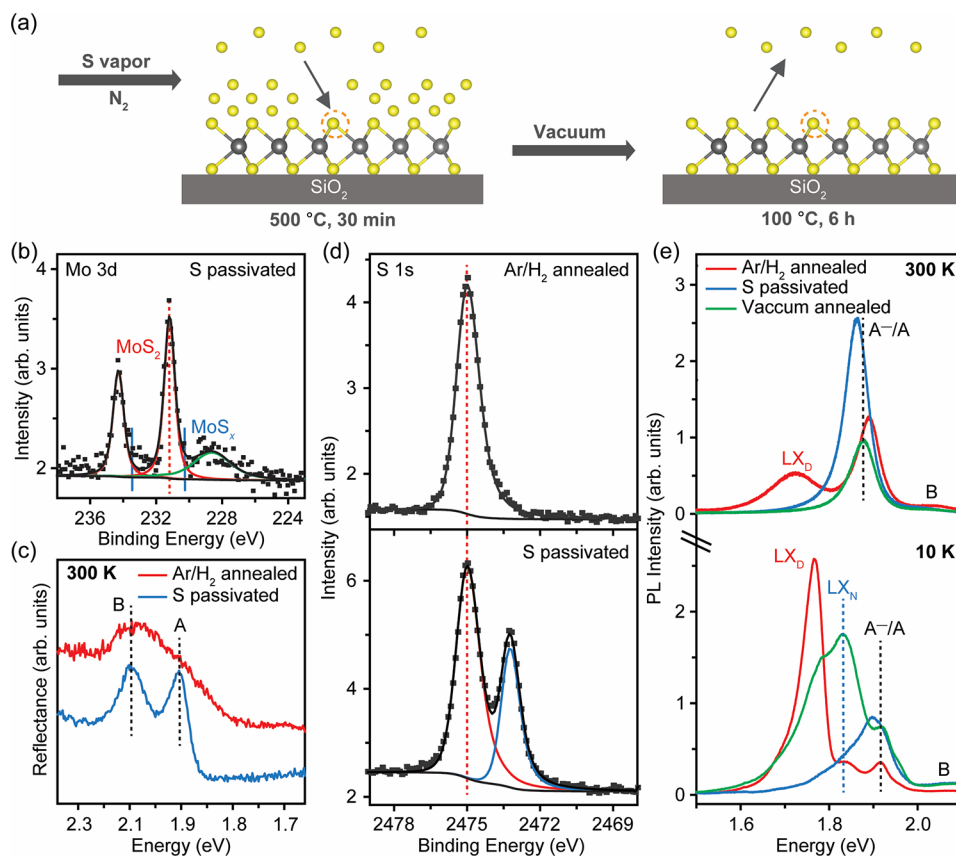


**Figure 5.** Sulfur passivation of Ar/H<sub>2</sub> annealed (600 °C, 30 min) monolayer MoS<sub>2</sub>. (a) Schematic of annealing the Ar/H<sub>2</sub> annealed (600 °C, 30 min) monolayer MoS<sub>2</sub> in sulfur vapor. (b) XPS spectra of Mo 3d in sulfur passivated monolayer MoS<sub>2</sub>. The absence of nonstoichiometric MoS<sub>x</sub> (denoted in blue) indicates the passivation of sulfur vacancies. (c) Reflectance spectra of sulfur passivated monolayer MoS<sub>2</sub> restoring to pristine with the A and B excitonic edges recovered. (d) XPS spectra of S 1s in Ar/H<sub>2</sub> annealed and sulfur passivated monolayer MoS<sub>2</sub> probed by synchrotron 3 keV hard X-rays. The Ar/H<sub>2</sub> annealed MoS<sub>2</sub> only shows a pristine S 1s peak (denoted in red), whereas the passivated MoS<sub>2</sub> shows two peaks. The second S 1s peak (denoted in blue) indicates the physisorbed sulfur on MoS<sub>2</sub> surface. (e) PL spectra of Ar/H<sub>2</sub> annealed (600 °C, 30 min), sulfur passivated, and vacuum annealed monolayer MoS<sub>2</sub>. At 300 K, the LX<sub>D</sub> is absent in both sulfur passivated and vacuum annealed monolayer MoS<sub>2</sub>. At 10 K, the LX<sub>D</sub> is still absent in sulfur passivated MoS<sub>2</sub> whereas it weakly reappears in vacuum annealed MoS<sub>2</sub>.

2D Semiconductor using a polydimethylsiloxane (PDMS)-assisted exfoliation method. Target flakes were dry-transferred onto SiO<sub>2</sub>/Si substrate and put in a 1 in. tube furnace. The samples were flowed with 450 sccm of N<sub>2</sub> (99.9999% purity) for 10 min to remove tube oxygen and then heated to 250 °C for 1 h under 100 sccm of N<sub>2</sub> to clean contaminants.

**CVD Growth.** Monolayer MoS<sub>2</sub> was grown by CVD using MoO<sub>3</sub> and sulfur powders as precursors. NaOH was dissolved in water with a concentration of 4 mg/mL and spin-coated on SiO<sub>2</sub>/Si wafers as a primer. Then 0.125 mg of MoO<sub>3</sub> and 30 mg of sulfur were placed in two alumina boats, respectively, in the center and upstream of the tube furnace. SiO<sub>2</sub>/Si wafers were placed face-down on top of MoO<sub>3</sub>. The furnace was heated to 700 °C and maintained for 10 min for the growth of MoS<sub>2</sub> layers. A 260/60 sccm of N<sub>2</sub> was used as carrier gas. Then the furnace was cooled down to RT, and samples are collected.

**Ar/H<sub>2</sub> Annealing.** Samples were flowed with 450 sccm Ar/H<sub>2</sub> (95%:5%) for 10 min to remove tube oxygen and heated to 200 °C under 70 sccm Ar/H<sub>2</sub> for 10 min to remove tube moisture. Then samples were heated to the target annealing temperature and kept there for the target time.

**Annealing in Sulfur Vapor for Passivation.** First, 8 mg of sulfur powders were put on the upstream of tube furnace and Ar/H<sub>2</sub> annealed samples were put in the center of furnace. Then the tube was flowed with 450 sccm of N<sub>2</sub> for 10 min to remove tube oxygen and then heated to the target annealing temperature under 50 sccm of N<sub>2</sub> and kept for 30 min.

**Vacuum Annealing.** Passivated samples were evacuated to <10<sup>−6</sup> mbar and then heated to 100 °C for 6 h.

After each annealing, the furnace was rapidly cooled back to RT, and samples were removed from the tube for measurement.

**Measurement.** Optical images of samples were taken on a Nikon Eclipse LV150N optical microscope.

RT Raman and steady-state PL spectra were collected on a Renishaw inVia confocal microscope using 532 nm laser excitation. RT PL images and time-resolved PL measurements were taken on a custom-built optical microscope setup. Excitation of 532 nm was provided. The wide-field image was acquired using a 60× objective on an EMCCD camera, and the PL lifetimes were measured using TCSPC electronics after filtering out using selective band-pass filter. Reflection microscopy was performed with the same setup for PL measurement, coupled to a monochromator. Images from variable wavelength excitation were provided in reflection geometry on a camera.

Cryogenic PL spectra, PL mapping, and time-resolved PL measurements were measured on a Kymera spectrometer and Janis (ST-500) cryostat with a closed-cycle helium refrigerator. Continuous wave 474 nm laser and pulsed 405 nm laser were used as excitations for PL spectra/mapping and time-resolved PL measurements, respectively. Long pass filters and tunable bandpass filters were used to select the peaks during time-resolved PL measurements.

XPS measurements were performed at the I09 beamline at Diamond Light Source, UK. Both soft (100–2100 eV) and hard (2.1–20 keV) X-rays were directed to the same spot on the sample.



The beam size was around 15  $\mu\text{m}$  by 35  $\mu\text{m}$ . The core level spectra of  $\text{MoS}_2$  were acquired at photon energy of 1 keV and S 1s spectra were collected with excitation energy of 3 keV. Samples were heated at 80  $^\circ\text{C}$  under  $10^{-7}$  mbar for 1 h to remove physisorbed species prior to loading into measurement chamber ( $10^{-10}$  mbar). The Fermi level was calibrated by using a clean Au foil in contact with the sample holder. The spectral resolution was determined by measuring and fitting the Fermi edge of a Au foil with a Gaussian broadened Fermi–Dirac distribution and was determined to be 0.28 and 0.21 eV for the 3 and 1 keV measurements, respectively.

## ASSOCIATED CONTENT

### Supporting Information

The Supporting Information is available free of charge at <https://pubs.acs.org/doi/10.1021/acsnano.3c02103>.

Raman spectra of monolayer  $\text{MoS}_2$  annealed through 300–600  $^\circ\text{C}$   $\text{Ar}/\text{H}_2$  annealing; synchrotron X-ray radiation damage tests of monolayer  $\text{MoS}_2$ ; deconvoluted RT PL spectra of pristine,  $\text{Ar}/\text{H}_2$  annealed, sulfur passivated, and vacuum annealed monolayer  $\text{MoS}_2$ ; Raman spectra of monolayer  $\text{MoS}_2$  annealed through 300–550  $^\circ\text{C}$   $\text{Ar}$ -only annealing; comparison of RT PL spectrum of monolayer  $\text{MoS}_2$  on pristine and 600  $^\circ\text{C}$   $\text{Ar}/\text{H}_2$  annealed  $\text{SiO}_2$  substrate; 10 K PL spectra of 600  $^\circ\text{C}$   $\text{Ar}/\text{H}_2$  annealed monolayer  $\text{MoS}_2$  with half and full hBN encapsulation; 10 K  $\text{LX}_{\text{D}}$  intensity map of 600  $^\circ\text{C}$   $\text{Ar}/\text{H}_2$  annealed monolayer  $\text{MoS}_2$ ; Raman spectra of 600  $^\circ\text{C}$   $\text{Ar}/\text{H}_2$  annealed  $\text{MoS}_2$  with different annealing times; power-dependent PL spectra of pristine, 30 min, and 2 h  $\text{Ar}/\text{H}_2$  annealed monolayer  $\text{MoS}_2$  measured at 10 K; RT PL spectra of CVD-grown monolayer  $\text{MoS}_2$  with defect generation and passivation; RT PL spectra of monolayer  $\text{WS}_2$ ,  $\text{MoSe}_2$ , and  $\text{WSe}_2$  through  $\text{Ar}/\text{H}_2$  annealing with different annealing temperatures and times (PDF)

## AUTHOR INFORMATION

### Corresponding Authors

**Manish Chhowalla** – Department of Materials Science & Metallurgy, University of Cambridge, Cambridge CB3 0FS, United Kingdom; [orcid.org/0000-0002-8183-4044](https://orcid.org/0000-0002-8183-4044); Email: [mc209@cam.ac.uk](mailto:mc209@cam.ac.uk)

**Yan Wang** – Department of Materials Science & Metallurgy, University of Cambridge, Cambridge CB3 0FS, United Kingdom; Email: [yw472@cam.ac.uk](mailto:yw472@cam.ac.uk)

### Authors

**Yiru Zhu** – Department of Materials Science & Metallurgy, University of Cambridge, Cambridge CB3 0FS, United Kingdom; [orcid.org/0000-0002-1774-5311](https://orcid.org/0000-0002-1774-5311)

**Juhwan Lim** – Department of Materials Science & Metallurgy, University of Cambridge, Cambridge CB3 0FS, United Kingdom; Cavendish Laboratory, University of Cambridge, Cambridge CB2 1TN, United Kingdom

**Zhepeng Zhang** – Department of Physics, National University of Singapore, 117551, Singapore; Present Address: Z.Z.: 476 Lomita Mall, Stanford, California, California 94305, United States

**Soumya Sarkar** – Department of Materials Science & Metallurgy, University of Cambridge, Cambridge CB3 0FS, United Kingdom; [orcid.org/0000-0002-9715-9004](https://orcid.org/0000-0002-9715-9004)

**Hugh Ramsden** – Department of Materials Science & Metallurgy, University of Cambridge, Cambridge CB3 0FS, United Kingdom; [orcid.org/0000-0002-0934-2088](https://orcid.org/0000-0002-0934-2088)

**Yang Li** – Department of Materials Science & Metallurgy, University of Cambridge, Cambridge CB3 0FS, United Kingdom; [orcid.org/0000-0003-2005-7381](https://orcid.org/0000-0003-2005-7381)

**Han Yan** – Department of Materials Science & Metallurgy, University of Cambridge, Cambridge CB3 0FS, United Kingdom

**Dibya Phuyal** – Department of Materials Science & Metallurgy, University of Cambridge, Cambridge CB3 0FS, United Kingdom; Division of Material and Nano Physics, Department of Applied Physics, KTH Royal Institute of Technology, Stockholm SE-106 91, Sweden; [orcid.org/0000-0003-0351-3138](https://orcid.org/0000-0003-0351-3138)

**Nicolas Gauriot** – Cavendish Laboratory, University of Cambridge, Cambridge CB2 1TN, United Kingdom; [orcid.org/0000-0001-7725-7208](https://orcid.org/0000-0001-7725-7208)

**Akshay Rao** – Cavendish Laboratory, University of Cambridge, Cambridge CB2 1TN, United Kingdom; [orcid.org/0000-0003-4261-0766](https://orcid.org/0000-0003-4261-0766)

**Robert L. Z. Hoyer** – Inorganic Chemistry Laboratory, Department of Chemistry, University of Oxford, Oxford OX1 3QR, United Kingdom; [orcid.org/0000-0002-7675-0065](https://orcid.org/0000-0002-7675-0065)

**Goki Eda** – Department of Physics, National University of Singapore, 117551, Singapore; Department of Chemistry, National University of Singapore, 117543, Singapore; Centre for Advanced 2D Materials, National University of Singapore, 117542, Singapore; [orcid.org/0000-0002-1575-8020](https://orcid.org/0000-0002-1575-8020)

Complete contact information is available at: <https://pubs.acs.org/doi/10.1021/acsnano.3c02103>

### Author Contributions

M.C. conceived the idea and supervised the project. Y.Z. and Y.W. designed the experiments, with suggestions from R.L.Z.H. around the concept of intentionally introducing defects through annealing. Y.Z. prepared samples, performed RT steady-state PL and Raman spectroscopy measurement. Y.W. and Y.L. fabricated In/Au electrodes and performed synchrotron XPS measurement with H.Y. and D.P.; J.L. and N.G. performed RT PL imaging, reflectance, and time-resolved PL spectroscopy measurement under A.R.'s supervision. Z.Z. performed cryogenic steady-state PL and time-resolved PL spectroscopy measurements under the supervision of G.E.; H.R. helped with the PL fitting to confirm the reproducibility of our method. All authors discussed the results and analysis. M.C., Y.Z., and S.S. wrote the manuscript, with input from all coauthors.

### Notes

The authors declare no competing financial interest.

## ACKNOWLEDGMENTS

We acknowledge funding from European Research Council (ERC) Advanced Grant under the European Union's Horizon 2020 research and innovation programme (grant agreement GA 101019828-2D-LOTTO), EPSRC (EP/T026200/1, EP/T001038/1), and the Royal Society Wolfson Merit Award (WRM/FT\180009). We acknowledge Diamond Light Source for time on beamline I09 under Proposal SI30105-1. We thank beamline scientists Tien-Lin Lee and Pardeep Kumar Thakur for their support. G.E. acknowledges support from the Ministry of Education (MOE), Singapore, under AcRF Tier 3 (MOE2018-T3-1-005). R.L.Z.H. thanks financial support

from the Royal Academy of Engineering through the Research Fellowships scheme (no. RF\201718\1701).

## REFERENCES

- (1) Liu, X.; Galfsky, T.; Sun, Z.; Xia, F.; Lin, E. C.; Lee, Y. H.; Kéna-Cohen, S.; Menon, V. M. Strong Light-Matter Coupling in Two-Dimensional Atomic Crystals. *Nat. Photonics* **2015**, *9*, 30–34.
- (2) Mak, K. F.; Lee, C.; Hone, J.; Shan, J.; Heinz, T. F. Atomically Thin  $\text{MoS}_2$ : A New Direct-Gap Semiconductor. *Phys. Rev. Lett.* **2010**, *105*, 136805.
- (3) Li, Y.; Chernikov, A.; Zhang, X.; Rigosi, A.; Hill, H. M.; van der Zande, A. M.; Chenet, D. A.; Shih, E. M.; Hone, J.; Heinz, T. F. Measurement of the Optical Dielectric Function of Monolayer Transition-Metal Dichalcogenides:  $\text{MoS}_2$ ,  $\text{MoSe}_2$ ,  $\text{WS}_2$ , and  $\text{WSe}_2$ . *Phys. Rev. B* **2014**, *90*, 205422.
- (4) Splendiani, A.; Sun, L.; Zhang, Y.; Li, T.; Kim, J.; Chim, C. Y.; Galli, G.; Wang, F. Emerging Photoluminescence in Monolayer  $\text{MoS}_2$ . *Nano Lett.* **2010**, *10*, 1271–1275.
- (5) Cao, T.; Wang, G.; Han, W.; Ye, H.; Zhu, C.; Shi, J.; Niu, Q.; Tan, P.; Wang, E.; Liu, B.; Feng, J. Valley-Selective Circular Dichroism of Monolayer Molybdenum Disulfide. *Nat. Commun.* **2012**, *3*, 887.
- (6) Regan, E. C.; Wang, D.; Paik, E. Y.; Zeng, Y.; Zhang, L.; Zhu, J.; MacDonald, A. H.; Deng, H.; Wang, F. Emerging Exciton Physics in Transition Metal Dichalcogenide Heterobilayers. *Nat. Rev. Mater.* **2022**, *7*, 778–795.
- (7) Lopez-Sanchez, O.; Lembke, D.; Kayci, M.; Radenovic, A.; Kis, A. Ultrasensitive Photodetectors Based on Monolayer  $\text{MoS}_2$ . *Nat. Nanotechnol.* **2013**, *8*, 497–501.
- (8) Hong, J.; Hu, Z.; Probert, M.; Li, K.; Lv, D.; Yang, X.; Gu, L.; Mao, N.; Feng, Q.; Xie, L.; et al. Exploring Atomic Defects in Molybdenum Disulfide Monolayers. *Nat. Commun.* **2015**, *6*, 6293.
- (9) Carozo, V.; Wang, Y.; Fujisawa, K.; Carvalho, B. R.; McCreary, A.; Feng, S.; Lin, Z.; Zhou, C.; Perea-López, N.; Elias, A. L.; et al. Optical Identification of Sulfur Vacancies: Bound Excitons at the Edges of Monolayer Tungsten Disulfide. *Sci. Adv.* **2017**, *3*, 1602813.
- (10) Vancsó, P.; Magda, G. Z.; Peto, J.; Noh, J. Y.; Kim, Y. S.; Hwang, C.; Biró, L. P.; Tapasztó, L. The Intrinsic Defect Structure of Exfoliated  $\text{MoS}_2$  Single Layers Revealed by Scanning Tunneling Microscopy. *Sci. Rep.* **2016**, *6*, 29726.
- (11) Refaely-Abramson, S.; Qiu, D. Y.; Louie, S. G.; Neaton, J. B. Defect-Induced Modification of Low-Lying Excitons and Valley Selectivity in Monolayer Transition Metal Dichalcogenides. *Phys. Rev. Lett.* **2018**, *121*, 167402.
- (12) Yang, J.; Wang, Y.; Lagos, M. J.; Manichev, V.; Fullon, R.; Song, X.; Voiry, D.; Chakraborty, S.; Zhang, W.; Batson, P. E.; Feldman, L.; Gustafsson, T.; Chhowalla, M. Single Atomic Vacancy Catalysis. *ACS Nano* **2019**, *13*, 9958–9964.
- (13) Mitterreiter, E.; Schuler, B.; Micevic, A.; Hernangómez-Pérez, D.; Barthelmi, K.; Cochrane, K. A.; Kiemle, J.; Sigger, F.; Klein, J.; Wong, E.; et al. The Role of Chalcogen Vacancies for Atomic Defect Emission in  $\text{MoS}_2$ . *Nat. Commun.* **2021**, *12*, 3822.
- (14) Komsa, H. P.; Kotakoski, J.; Kurasch, S.; Lehtinen, O.; Kaiser, U.; Krasheninnikov, A. V. Two-Dimensional Transition Metal Dichalcogenides under Electron Irradiation: Defect Production and Doping. *Phys. Rev. Lett.* **2012**, *109*, 035503.
- (15) García-Esparza, A. T.; Park, S.; Abroshan, H.; Paredes Mellone, O. A.; Vinson, J.; Abraham, B.; Kim, T. R.; Nordlund, D.; Gallo, A.; Alonso-Mori, R.; Zheng, X.; Sokaras, D. Local Structure of Sulfur Vacancies on the Basal Plane of Monolayer  $\text{MoS}_2$ . *ACS Nano* **2022**, *16*, 6725–6733.
- (16) Grünleitner, T.; Henning, A.; Bissolo, M.; Zengerle, M.; Gregoratti, L.; Amati, M.; Zeller, P.; Eichhorn, J.; Stier, A. V.; Holleitner, A. W.; Finley, J. J.; Sharp, I. D. Real-Time Investigation of Sulfur Vacancy Generation and Passivation in Monolayer Molybdenum Disulfide via *in situ* X-Ray Photoelectron Spectromicroscopy. *ACS Nano* **2022**, *16*, 20364–20375.
- (17) Ghorbani-Asl, M.; Kretschmer, S.; Spearot, D. E.; Krasheninnikov, A. V. Two-Dimensional  $\text{MoS}_2$  under Ion Irradiation: From Controlled Defect Production to Electronic Structure Engineering. *2D Mater.* **2017**, *4*, 025078.
- (18) Thiruraman, J. P.; Masih Das, P.; Drndić, M. Irradiation of Transition Metal Dichalcogenides Using a Focused Ion Beam: Controlled Single-Atom Defect Creation. *Adv. Funct. Mater.* **2019**, *29*, 1904668.
- (19) Koperski, M.; Nogajewski, K.; Arora, A.; Cherkez, V.; Mallet, P.; Veuillen, J. Y.; Marcus, J.; Kossacki, P.; Potemski, M. Single Photon Emitters in Exfoliated  $\text{WSe}_2$  Structures. *Nat. Nanotechnol.* **2015**, *10*, 503–506.
- (20) Parto, K.; Azzam, S. I.; Banerjee, K.; Moody, G. Defect and Strain Engineering of Monolayer  $\text{WSe}_2$  Enables Site-Controlled Single-Photon Emission up to 150 K. *Nat. Commun.* **2021**, *12*, 3585.
- (21) Li, L.; Qin, Z.; Ries, L.; Hong, S.; Michel, T.; Yang, J.; Salameh, C.; Bechelany, M.; Miele, P.; Kaplan, D.; Chhowalla, M.; Voiry, D. Role of Sulfur Vacancies and Undercoordinated Mo Regions in  $\text{MoS}_2$  Nanosheets toward the Evolution of Hydrogen. *ACS Nano* **2019**, *13*, 6824–6834.
- (22) Lin, L.; Miao, N.; Huang, J.; Zhang, S.; Zhu, Y.; Horsell, D. D.; Ghosez, P.; Sun, Z.; Allwood, D. A. A Photocatalyst of Sulphur Depleted Monolayered Molybdenum Sulfide Nanocrystals for Dye Degradation and Hydrogen Evolution Reaction. *Nano Energy* **2017**, *38*, 544–552.
- (23) Zhang, Q.; Wee, A. T. S.; Liang, Q.; Zhao, X.; Liu, M. Defect Engineering of Two-Dimensional Transition-Metal Dichalcogenides: Applications, Challenges, and Opportunities. *ACS Nano* **2021**, *15*, 2165–2181.
- (24) Lee, J.-Y.; Kim, J. H.; Jung, Y.; Shin, J. C.; Lee, Y.; Kim, K.; Kim, N.; van der Zande, A. M.; Son, J.; Lee, G.-H. Evolution of Defect Formation during Atomically Precise Desulfurization of Monolayer  $\text{MoS}_2$ . *Commun. Mater.* **2021**, *2*, 80.
- (25) Lu, J.; Carvalho, A.; Chan, X. K.; Liu, H.; Liu, B.; Tok, E. S.; Loh, K. P.; Castro Neto, A. H.; Sow, C. H. Atomic Healing of Defects in Transition Metal Dichalcogenides. *Nano Lett.* **2015**, *15*, 3524–3532.
- (26) Shen, P. C.; Lin, Y.; Su, C.; McGahan, C.; Lu, A. Y.; Ji, X.; Wang, X.; Wang, H.; Mao, N.; Guo, Y.; et al. Healing of Donor Defect States in Monolayer Molybdenum Disulfide Using Oxygen-Incorporated Chemical Vapour Deposition. *Nat. Electron.* **2022**, *5*, 28–36.
- (27) Bretscher, H.; Li, Z.; Xiao, J.; Qiu, D. Y.; Refaely-Abramson, S.; Alexander-Webber, J. A.; Tanoh, A.; Fan, Y.; Delport, G.; Williams, C. A.; Stranks, S. D.; Hofmann, S.; Neaton, J. B.; Louie, S. G.; Rao, A. Rational Passivation of Sulfur Vacancy Defects in Two-Dimensional Transition Metal Dichalcogenides. *ACS Nano* **2021**, *15*, 8780–8789.
- (28) Verhagen, T.; Guerra, V. L. P.; Haider, G.; Kalbac, M.; Vejpravova, J. Towards the Evaluation of Defects in  $\text{MoS}_2$  Using Cryogenic Photoluminescence Spectroscopy. *Nanoscale* **2020**, *12*, 3019–3028.
- (29) Goodman, A. J.; Willard, A. P.; Tisdale, W. A. Exciton Trapping Is Responsible for the Long Apparent Lifetime in Acid-Treated  $\text{MoS}_2$ . *Phys. Rev. B* **2017**, *96*, 121404.
- (30) Zhang, Z.; Liang, H.; Loh, L.; Chen, Y.; Chen, Y.; Watanabe, K.; Taniguchi, T.; Quek, S. Y.; Bosman, M.; Bettiol, A. A.; Eda, G. Optically Active Chalcogen Vacancies in Monolayer Semiconductors. *Adv. Opt. Mater.* **2022**, *10*, 2201350.
- (31) Sarkar, S.; Goswami, S.; Trushin, M.; Saha, S.; Panahandeh-Fard, M.; Prakash, S.; Tan, S. J. R.; Scott, M.; Loh, K. P.; Adam, S.; Mathew, S.; Venkatesan, T. Polaronic Trions at the  $\text{MoS}_2/\text{SrTiO}_3$  Interface. *Adv. Mater.* **2019**, *31*, 1903569.
- (32) Bae, S.; Sugiyama, N.; Matsuo, T.; Raebiger, H.; Shudo, K. I.; Ohno, K. Defect-Induced Vibration Modes of  $\text{Ar}^+$ -Irradiated  $\text{MoS}_2$ . *Phys. Rev. Appl.* **2017**, *7*, 024001.
- (33) Mignuzzi, S.; Pollard, A. J.; Bonini, N.; Brennan, B.; Gilmore, I. S.; Pimenta, M. A.; Richards, D.; Roy, D. Effect of Disorder on Raman Scattering of Single-Layer  $\text{MoS}_2$ . *Phys. Rev. B* **2015**, *91*, 195411.
- (34) Wang, Y.; Kim, J. C.; Wu, R. J.; Martinez, J.; Song, X.; Yang, J.; Zhao, F.; Mkhoyan, A.; Jeong, H. Y.; Chhowalla, M. Van Der Waals Contacts between Three-Dimensional Metals and Two-Dimensional Semiconductors. *Nature* **2019**, *568*, 70–74.



- (35) Kondekar, N. P.; Boebinger, M. G.; Woods, E. V.; McDowell, M. T. *In situ* XPS Investigation of Transformations at Crystallographically Oriented MoS<sub>2</sub> Interfaces. *ACS Appl. Mater. Interfaces* **2017**, *9*, 32394–32404.
- (36) Scofield, J. H. *Theoretical Photoionization Cross Sections from 1 to 1500 KeV*; Report No. UCRL-51326; Lawrence Livermore Laboratory, California University: Livermore, CA, 1973.
- (37) Kolobov, A. V.; Tominaga, J. Two-Dimensional Transition-Metal Dichalcogenides. *Springer Ser. Mater. Sci.* **2016**, *239*, 148–153.
- (38) Liu, M.; Shi, J.; Li, Y.; Zhou, X.; Ma, D.; Qi, Y.; Zhang, Y.; Liu, Z. Temperature-Triggered Sulfur Vacancy Evolution in Monolayer MoS<sub>2</sub>/Graphene Heterostructures. *Small* **2017**, *13*, 1602967.
- (39) Zhao, Y.; Tripathi, M.; Čerņevičs, K.; Avsar, A.; Ji, H. G.; Gonzalez Marin, J. F.; Cheon, C. Y.; Wang, Z.; Yazyev, O. V.; Kis, A. Electrical Spectroscopy of Defect States and Their Hybridization in Monolayer MoS<sub>2</sub>. *Nat. Commun.* **2023**, *14*, 44.
- (40) Zhou, W.; Zou, X.; Najmaei, S.; Liu, Z.; Shi, Y.; Kong, J.; Lou, J.; Ajayan, P. M.; Yakobson, B. I.; Idrobo, J. C. Intrinsic Structural Defects in Monolayer Molybdenum Disulfide. *Nano Lett.* **2013**, *13*, 2615–2622.
- (41) Frisenda, R.; Niu, Y.; Gant, P.; Molina-Mendoza, A. J.; Schmidt, R.; Bratschitsch, R.; Liu, J.; Fu, L.; Dumcenco, D.; Kis, A.; De Lara, D. P.; Castellanos-Gomez, A. Micro-Reflectance and Transmittance Spectroscopy: A Versatile and Powerful Tool to Characterize 2D Materials. *J. Phys. D: Appl. Phys.* **2017**, *50*, 074002.
- (42) Mak, K. F.; He, K.; Lee, C.; Lee, G. H.; Hone, J.; Heinz, T. F.; Shan, J. Tightly Bound Trions in Monolayer MoS<sub>2</sub>. *Nat. Mater.* **2013**, *12*, 207–211.
- (43) Klein, J.; Sigl, L.; Gyger, S.; Barthelmi, K.; Florian, M.; Rey, S.; Taniguchi, T.; Watanabe, K.; Jahnke, F.; Kastl, C.; Zwiller, V.; Jöns, K. D.; Müller, K.; Wurstbauer, U.; Finley, J. J.; Holleitner, A. W. Engineering the Luminescence and Generation of Individual Defect Emitters in Atomically Thin MoS<sub>2</sub>. *ACS Photonics* **2021**, *8*, 669–677.
- (44) Wierzbowski, J.; Klein, J.; Sigger, F.; Straubinger, C.; Kremser, M.; Taniguchi, T.; Watanabe, K.; Wurstbauer, U.; Holleitner, A. W.; Kaniber, M.; et al. Direct Exciton Emission from Atomically Thin Transition Metal Dichalcogenide Heterostructures near the Lifetime Limit. *Sci. Rep.* **2017**, *7*, 12383.
- (45) Yagodkin, D.; Greben, K.; Eljarrat, A.; Kovalchuk, S.; Ghorbani-Asl, M.; Jain, M.; Kretschmer, S.; Severin, N.; Rabe, J. P.; Krasheninnikov, A. V.; Koch, C. T.; Bolotin, K. I. Extrinsic Localized Excitons in Patterned 2D Semiconductors. *Adv. Funct. Mater.* **2022**, *32*, 2203060.
- (46) Wang, H.; Zhang, C.; Chan, W.; Manolatu, C.; Tiwari, S.; Rana, F. Radiative Lifetimes of Excitons and Trions in Monolayers of the Metal Dichalcogenide MoS<sub>2</sub>. *Phys. Rev. B* **2016**, *93*, 045407.
- (47) Kaplan, D.; Mills, K.; Lee, J.; Torrel, S.; Swaminathan, V. Excitation Intensity Dependent Photoluminescence of Annealed Two-Dimensional MoS<sub>2</sub> Grown by Chemical Vapor Deposition. *J. Appl. Phys.* **2016**, *119*, 214301.
- (48) Tongay, S.; Suh, J.; Ataca, C.; Fan, W.; Luce, A.; Kang, J. S.; Liu, J.; Ko, C.; Raghunathan, R.; Zhou, J.; et al. Defects Activated Photoluminescence in Two-Dimensional Semiconductors: Interplay between Bound, Charged, and Free Excitons. *Sci. Rep.* **2013**, *3*, 2657.
- (49) Srivastava, A.; Sidler, M.; Allain, A. V.; Lembke, D. S.; Kis, A.; Imamoglu, A. Optically Active Quantum Dots in Monolayer WSe<sub>2</sub>. *Nat. Nanotechnol.* **2015**, *10*, 491–496.
- (50) Bowker, M.; Madix, R. J. UPS and Thermal Desorption Studies of Alcohol Adsorption on Cu (110): I. Methanol. *Surf. Sci.* **1980**, *95*, 190–206.

## Recommended by ACS

### Electroluminescence from Megasonically Solution-Processed MoS<sub>2</sub> Nanosheet Films

Sonal V. Rangnekar, Mark C. Hersam, *et al.*

AUGUST 22, 2023  
ACS NANO

READ 

### One-Step Passivation of Both Sulfur Vacancies and SiO<sub>2</sub> Interface Traps of MoS<sub>2</sub> Device

Byungwook Ahn, Seong Chu Lim, *et al.*

AUGUST 30, 2023  
NANO LETTERS

READ 

### Identification of Ubiquitously Present Polymeric Adlayers on 2D Transition Metal Dichalcogenides

Rita Tilmann, Georg S. Duesberg, *et al.*

MAY 23, 2023  
ACS NANO

READ 

### Self-Limiting Growth of Monolayer Tungsten Disulfide Nanoribbons on Tungsten Oxide Nanowires

Hiroo Suzuki, Yasuhiko Hayashi, *et al.*

MAY 01, 2023  
ACS NANO

READ 

Get More Suggestions >